Gas Sensing Properties of p-Co$_3$O$_4$/n-TiO$_2$ Nanotube Heterostructures

Onur Alev, Alp Kılıç, Çiğdem Çakırlar, Serkan Büyükköse and Zafer Ziya Öztürk *

Department of Physics, Gebze Technical University, 41400 Kocaeli, Turkey; onuralev@gtu.edu.tr (O.A.); akilic@gtu.edu.tr (A.K.); ccakirlar@gtu.edu.tr (Ç.Ç.); sbuyukkose@gtu.edu.tr (S.B.)

* Correspondence: zozturk@gtu.edu.tr

Abstract: In this paper, we fabricated p-Co$_3$O$_4$/n-TiO$_2$ heterostructures and investigated their gas sensing properties. The structural and morphological characterization were performed by scanning electron microscopy (SEM), X-ray diffraction (XRD), and X-ray photoelectron spectroscopy analysis (XPS). The electrical properties of the heterostructure were studied within the temperature range from 293 K to 423 K. Changes in electrical properties and sensing behavior against reducing and oxidizing gases were attributed to the formation of p–n heterojunctions at the Co$_3$O$_4$ and TiO$_2$ interface. In comparison with sensing performed with pristine TiO$_2$ nanotubes (NTs), a significant improvement in H$_2$ sensing at 200 °C was observed, while the sensing response against NO$_2$ decreased for the heterostructures. Additionally, a response against toluene gas, in contrast to pristine TiO$_2$ NTs, appeared in the Co$_3$O$_4$/TiO$_2$ heterostructure samples.

Keywords: metal-oxide; gas sensor; nanostructures; heterostructure; nanotubes; TiO$_2$; Co$_3$O$_4$

1. Introduction

Metal-oxide (MOX)-based gas sensors have a wide range of applications such as medical, air quality, energy efficiency, and the detection of hazardous gases. MOXs are preferred for sensing layers due to their easy fabrication, low cost, high sensor response, and easy integration [1]. Moreover, device performance is improved when sensors are fabricated with nanostructured MOXs. However, for almost all sensor applications, there is a strong demand for better sensor properties such as lower operation temperature and higher sensitivity and selectivity [2,3]. Different techniques, such as doping, loading, or heterostructure fabrication, have been employed to meet these requirements [4–8]. Among them, the combination of n-type and p-type MOX materials in the form of nanostructures is one of the most promising techniques [6,9]. An extended depletion layer between two different types of MOX semiconductors can provide higher sensor properties [9].

This study is focused on the combination of p-type cobalt oxide (Co$_3$O$_4$) and n-type TiO$_2$. TiO$_2$ is a very important material, especially for the sensing of H$_2$ and VOCs, due to its high sensitivity and easy nanostructure fabrication [10–15]. Co$_3$O$_4$, well known as a catalytic activator in chemical processes such as oxidation reactions, has a great potential for sensor applications [16–19]. p-type Co$_3$O$_4$ can advance the sensing capabilities of TiO$_2$ nanostructures. In this study, different amounts of Co$_3$O$_4$ were loaded on TiO$_2$ nanotubes (NTs) to understand the heterostructure effect on sensing properties. The heterostructures were fabricated by a two-step electrochemical process. TiO$_2$ NTs were fabricated via an anodization process and Co$_3$O$_4$ was loaded onto the NTs via electrochemical deposition. Then, electrical and sensor measurements were carried out.

2. Experiment

Co_3O_4/TiO_2 heterostructures were fabricated via two-step electrochemical deposition consisting of anodization and cathodic deposition. Ti foils (20 mm in length and 10 mm in width) were provided from Sigma-Aldrich (St. Louis, MO, USA). NH_4F (ammonium fluoride, 99.99%), ethylene glycol (99.8%), and cobalt (II) nitrate hexahydrate (99.999%) were purchased from Sigma-Aldrich. Ultra-pure (UP) water was used for all experiments. In the first step, Ti foils were cleaned with acetone, isopropanol, and UP water in ultrasonic bath, respectively. Then, the foils were dried in a nitrogen stream. An electrolyte solution was prepared with NH_4F, ethylene glycol, and UP water with a molar ratio of 0.25:2:100. The anodization was carried out at 50 V with Pt foil as cathode in a thermos-stated bath at 20 °C for 1 h. Afterward, Co_3O_4 was loaded on TiO_2 NTs (set as cathode) via cathodic deposition. The electrolyte for cathodic deposition was composed of 0.01 wt % cobalt (II) nitrate hexahydrate in UP water. Cathodic deposition was performed under three different conditions (5 V for 3 min, 10 V for 1 min, and 10 V for 3 min), and the resulting samples were named and are hereafter referred to as CT-1, CT-2, and CT-3, respectively. After the fabrication of Co_3O_4/TiO_2 heterostructures, samples were rinsed with UP water and dried under a nitrogen stream. Finally, the fabricated samples were annealed at 500 °C for 3 h in an oxygen atmosphere to obtain a crystalline structure.

To investigate the crystal structure and morphological properties of the fabricated samples, XRD, SEM, and XPS methods were used.

Current–voltage (*I–V*) measurements were performed in the temperature range of 20–200 °C to investigate the electrical properties of fabricated samples. Au electrodes 100 nm thick were thermally evaporated on top of the fabricated samples as shown in Figure 1a,b. Because of the geometry of the devices, measurements were performed for vertical configuration (contacts are on top of the NTs and on Ti foil). A Keithley electrometer, model 6517 A, was used for electrical measurements with a Lakeshore 340 temperature controller. *I–V* curves were obtained by a linear voltage sweep between −1 V and +1 V with a scan rate of 0.05 V.
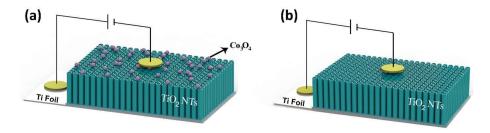

Figure 1. Measurement scheme of (**a**) pristine TiO_2 nanotubes (NTs) and (**b**) Co_3O_4/TiO_2 heterostructures.

Pristine TiO_2 and Co_3O_4/TiO_2 heterostructure sensors were investigated toward H_2, NO_2, and VOCs (ethanol, acetone, toluene, and xylene). The sensors were mounted in a homemade test chamber with a volume of 1 L. Desired H_2 and NO_2 gas concentrations were obtained from gas tubes via mass flow controllers. VOCs were generated from cooled bubblers immersed in a thermal bath with dry air as a carrier gas [20]. Concentration of the VOCs were calculated using Antoine's equation [21]. Baseline signal of the sensor was determined under dry air flow conditions. After the exposure to the target gases, recovery of the sensor from saturated conditions was achieved under dry airflow. Sensor measurements are presented in terms of sensor response, defined as $R_s = \Delta I/I_0$, where ΔI is the change in current. Here, R_s is defined for reducing gases such as H_2 and VOCs, and ΔI is given as $I_g - I_0$. For oxidizing gases, such as NO_2, sensor response is defined slightly differently: $R_s = \Delta I/I_g$. Here, ΔI is given as $I_0 - I_g$. For both formulations, I_g is the current after the sensor is exposed to the reducing or oxidizing analyte gas, and I_0 is the reference value (baseline current) of the sensor exposed to high-purity dry air.

3. Results and Discussion

Corresponding reactions for TiO_2 and Co_3O_4 formation in the two-step electrodeposition route can be given as follows [17,22,23]:

$$2H_2O \rightarrow O_2 + 4e^- + 4H^+ \tag{1a}$$

$$Ti + O_2 \rightarrow TiO_2 \tag{1b}$$

$$CO_3O_4 + H_2O + OH^- \leftrightarrow 3CoOOH + e^- \tag{2a}$$

$$CoOOH + OH^- \leftrightarrow CoO_2 + H_2O + e^-. \tag{2b}$$

Figure 2 shows SEM images of fabricated structures. Figure 2a indicates that a film of vertically aligned TiO_2 NTs homogeneously covers the surface. The average NT diameter is 80 nm as seen in Figure 2a inset. Figure 2b–d shows cathodically deposited particles on the NTs. In the cathodic process, the amount of deposited Co_3O_4 changes with bias voltage and process time. Thin film formation was observed for CT-3, which was grown with a 10 V bias voltage and a 3 min process time (Figure 2d). EDS mapping and spectrums of CT-1 and CT-3 are given in Figure 3. The presence of the Co, Ti, and O was observed. XRD patterns of pristine TiO_2 NTs and Co_3O_4/TiO_2 heterostructures are given in Figure 4. The XRD patterns reveal that all diffraction peaks could be indexed to Ti and anatase TiO_2 NTs [20]. According to the XRD results, Co_3O_4 particles on the surface most likely do not have crystalline structures. Even if there is a small degree of crystallinity for Co_3O_4 at 36.32°, the TiO_2 reflection overlaps with that of the Co_3O_4, thus preventing any clearly visible peak from the rest of the signal [24].
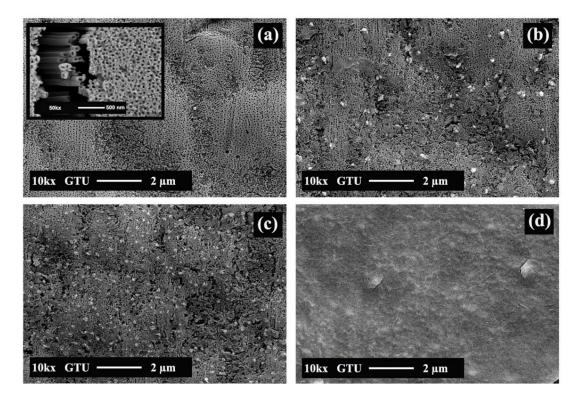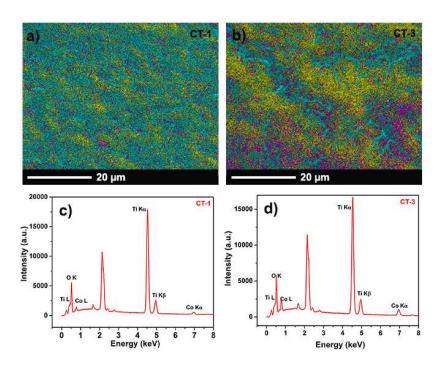

Figure 2. SEM images of (**a**) pristine TiO_2 NTs, (**b**) CT-1, (**c**) CT-2, and (**d**) CT-3.

Figure 3. EDS mapping results of (**a**) CT-1 and (**b**) CT-3 sample, and EDS spectrum of (**c**) CT-1 and (**d**) CT-3 samples. In the mapping results, yellow represents O, blue represents Ti, and purple represents Co.
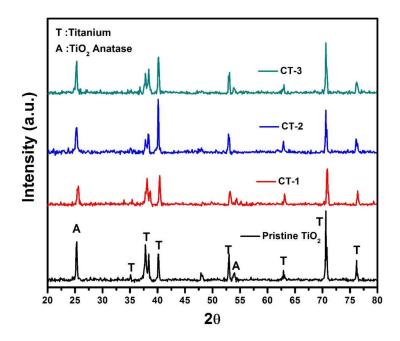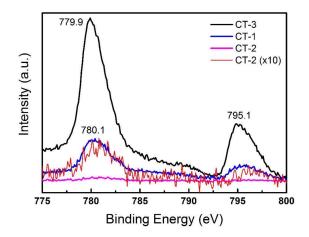

Figure 4. XRD patterns of pristine TiO_2, CT-1, CT-2, and CT-3 samples.

To identify the surface chemical compositions and oxidation states of the NTs after Co deposition, X-ray photoelectron spectroscopy (XPS) was performed. CT-2 spectra shows Ti 2p and O 1s peaks originating from the TiO_2 NTs. However, the Co 2p peak is very weak and can only be seen when the data is magnified ($\times 10$), which will be shown in the high-resolution XPS spectrum of the Co 2p region (Figure 5). This implies that the Co oxide coverage is very low in this sample. The presence of Co, in addition to the presence of Ti and O, is visible in the spectrum of CT-1, which indicates that the coverage is more pronounced in this sample. On the other hand, the CT-3 survey scan shows a more intense peak for Co 2p but not for Ti 2p, indicating that the surface is fully covered by cobalt oxide,

which means that TiO_2 NTs are too far under the surface to detect. SEM images of CT-1, CT-2, and CT-3 in Figure 2 support these findings. CT-1 and CT-2 show islands of Co_3O_4 on TiO_2 NTs, whereas a full coverage is clear in CT-3.

Figure 5. XPS spectra of Co 2p spectra of CT-1 (blue), CT-2 (red), and CT-3 (black). The intensity of CT-2 was magnified $10\times$ (pink) for clarity.

Figure 5 shows Co 2p spectra of CT-1, CT-2 and CT-3. CT-1 and CT-2 spectra show two peaks at binding energies of 780.1 eV and 795.1 eV, corresponding to Co 2p3/2 and Co 2p1/2 peaks, implying a Co_3O_4 form [25]. The peak intensity of CT-2 is lower than CT-1 (the intensity of CT-2 is magnified $10\times$ for clarity in Figure 4), indicating lower coverage compared to CT-1. The Co peak intensity of CT-3 is the highest, which was expected from the complete Co_3O_4 layer. The Co 2p3/2 peak of CT-3 shifted to 779.9 eV, which can be attributed to the increase in Co_3O_4 coverage from the sub-monolayer to the multilayer, resulting in a change in the local electronic properties and bonding geometries. Similar shifts have been observed in TiO_2 and Al_2O_3 films as well [26–28].

Figure 6 shows the high-resolution XPS spectrum of the O 1s regions for CT-1, CT-2, and CT-3, all of which can be fitted into two peaks. CT-1 and CT-2 show a primary peak at 530.5 eV, which can be attributed to the O–Ti bond in TiO_2 [25]. The smaller secondary peaks at 532.3 eV and 531.1 eV in CT-2 and CT-1, respectively, can both be attributed to the O in Co_3O_4. In CT-1, the difference in peak height between the 530.5 eV peak and the secondary peak is higher compared to that in CT-2, suggesting that the Co_3O_4 contribution is less in this sample compared to CT-1, indicative of less Co_3O_4 coverage. In CT-3, where the surface is fully covered with Co_3O_4, the peak position of the Co–O bond is shifted from 531.1 eV to 529.9 eV and becomes the primary peak, possibly due to the Co_3O_4 coverage from the sub-monolayer to the multilayer. The small changes in the geometry of the film and the changes in the local electronic properties and bonding geometries could be the main contributor to the shift. Similar shifts have been observed for TiO_2 and Al_2O_3 films as well [26–28]. The peak at 530.9 eV is attributed to the O–H group in the Co hydroxide precursor [25].

Electrical characterization was performed under the condition and parameters as given in our previous work [29]. Electrical resistance of the heterostructures given in Figure 7a shows an increment with the loading of Co_3O_4. This behavior is attributed to the modification of the conduction channel by the depletion of charge carriers at the heterojunction interface. This mechanism, as discussed later in this text, is also responsible for the enhanced sensor performance of the heterostructures in terms of reducing gases. The *I–V* curves measured at 200 °C are given in Figure 7b.
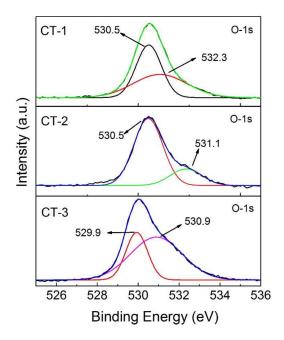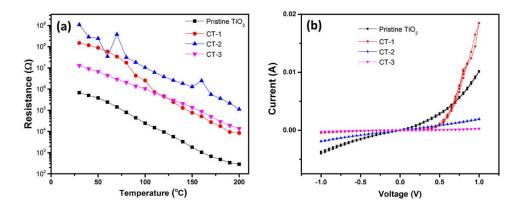
Figure 6. XPS spectra of the O 1s regions of CT-1, CT-2, and CT-3.

Figure 7. (**a**) Resistance vs. temperature of the sensors and (**b**) *I–V* curves at 200 °C.

Amperometric sensor measurements of H_2, VOCs (ethanol, acetone, toluene, xylene, and chloroform), and NO_2 were performed under a constant voltage at different operation temperatures. The gas sensing responses of samples at 200 °C are shown in Figure 8. These data confirm the absence of sensitivity toward acetone and ethanol for Co_3O_4/TiO_2 heterostructures, while TiO_2 NTs could sense both VOCs. On the other hand, the sensor response to hydrogen increased with Co_3O_4/TiO_2 heterostructures. The CT-1 sample, compared to the sample of pristine TiO_2 NTs, showed an approximately nine-fold higher response to H_2. In addition, the response to toluene starts to appear after Co_3O_4 loading. Sensor responses to 1000 ppm H_2 in 50% relative humidity (RT) can be seen in Figure 8. It is well known that the presence of humidity can cause a deterioration in sensor properties [30]. Despite the relative magnitudes of heterostructure sensor responses, compared with those of pristine TiO_2, to pure H_2 and H_2/humidity mixtures, there was no significant improvement observed when humidity was eliminated (Figure 8). In addition to H_2 and VOCs, sensors responses to 50 ppm NO_2 are given in Figure 7. The sensor responses are 17, 0.02, 1.32, 3.3 for pristine TiO_2, CT-1, CT-2, and CT-3, respectively.
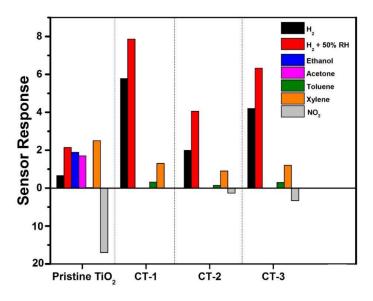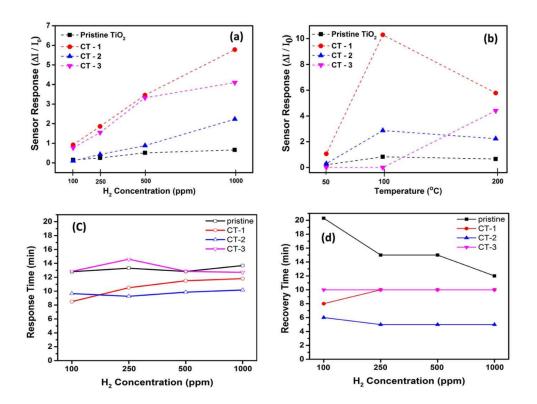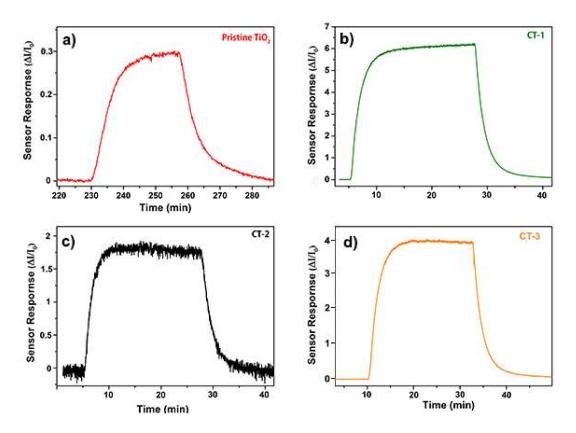
Figure 8. Sensor responses to 1000 ppm H_2 and VOCs and to 50 ppm NO_2 at an operation temperature of 200 °C.

Figure 9a shows sensor responses for different H_2 concentrations at 200 °C. Co_3O_4-loaded samples could detect lower H_2 concentrations than pristine TiO_2 could. The CT-1 sample exhibited the highest sensor responses at every concentration of H_2. Sensor response vs. temperature graph was given in Figure 9b. The CT-1 sample showed better sensor responses at all temperatures. Although the CT-1 sample showed the highest sensor response at 100 °C, a better response time and recovery time for CT-1 were observed at 200 °C (data not shown). Dynamic sensor responses can be seen in Figure 10. It is obvious that, to obtain the best sensor performance from these devices, operation temperature is a critical variable, and its optimum value will be different for each device. Regarding the response time and recovery time, the loaded samples exhibited lower values and thus better performance than did the pristine TiO_2 NTs, as can be seen in Figure 9c,d.

Based on the above results, Co_3O_4-loaded TiO_2 NTs heterostructures showed enhanced sensor properties compared to the pristine TiO_2 NT sensor. Sensing mechanisms of MOX sensors that are composed of only p-type or n-type materials have been studied and well explained in the literature [31–35]. Enhanced sensor properties can be attributed to variation in the resistance by the formation of the p–n junction [35]. Even though there is no readily accepted and developed mechanism with detailed sensing treatment for heterostructures, two considerations might be taken into account as responsible mechanisms. The first one is the catalytic effect of Co_3O_4. In this case, Co_3O_4 plays a role as a catalyst material in the reaction between analyte gas and TiO_2 [36]. If a continuous film is formed on the surface, a catalytic role of the Co_3O_4 turns into a sensing layer, so a lower sensor performance generally is observed [37]. This idea is also supported by the sensing behavior of the CT-3 sensor response (in Figure 9) and by the XPS and SEM data that indicate full coverage on the surface for CT-3. Previous works have reported the enhanced sensor properties due to the catalyst role and hydrogen sensitivity of Co_3O_4 [16,38,39].

Figure 9. (**a**) Sensor response vs. H_2 concentration at 200 °C. (**b**) Sensor response vs. operation temperature for 1000 ppm H_2. (**c**) Response time vs. H_2 concentration at 200 °C. (**d**) Recovery time vs. H_2 concentration at 200 °C.

Figure 10. Sensor response versus time graphs of (**a**) pristine TiO_2, (**b**) CT-1, (**c**) CT-2, and (**d**) CT-3 to 1000 ppm H_2 at 200 °C.

Another possible mechanism that is responsible for the enhanced performance of the sensors is the formation of the p–n junction at the interface between p-type Co_3O_4 and n-type TiO_2 [31,39]. This formation is partially observed on electrical measurements with an increase in the resistance with Co_3O_4 loading (Figure 7). Especially, the CT-1 sensor that exhibits optimal sensor properties evidently showed diode-like rectifying behavior. Due to the depletion region at the heterojunction interface, which causes a narrower cross-sectional area for charge carriers in the nanorod, an increase in resistance is observed. A reduced cross-sectional area available for charge conduction in the nanowire will result in increased resistance. When reducing gases such as VOCs or H_2 are introduced, gas molecules can diffuse into the interface, modify the junction, and thus enhance the sensor response by decreasing the initially high resistance value because of the released electrons into the junction [5]. A relatively easy diffusion of H_2 molecules into the interface, appears as sensing selectivity against H_2 in Figure 8 [40]. Contrary to reducing gases, introduction of an oxidizing gas such as NO_2 will give an additional increase in resistance due to a further widening of the depletion region. However, a tendency for the resistance to further increase will not appear noticeably in sensor response due to the presence of exceedingly high resistance. This mechanism well explains the difference in response data of our samples with respect to reducing and oxidizing gases, given in Figure 8. Another important parameter of the electrical behavior of the p–n junction is operation temperature because of its role in carrier concentration. Its effect appears prominently in Figure 9b.

4. Conclusions

p-Co_3O_4/n-TiO_2 heterostructures were fabricated via a two-step electrochemical process involving anodization and cathodic deposition. The structure and morphology of the heterostructures were characterized by SEM, XRD, and XPS, which confirms that Co_3O_4 particles were spread uniformly over the TiO_2 NT surface. Changes in electrical resistance and *I–V* curves partially support the p–n junction formation. The p-Co_3O_4/n-TiO_2 heterostructures, in comparison with those of the pristine TiO_2 NTs, show significantly improved H_2 sensing response at 200 °C, which is an up to 9-fold increase. Co_3O_4 loading also provides a sensing response against toluene. In contrast, sensing response against NO_2 decreased for Co_3O_4-loaded samples. This difference in sensor behavior against reducing and oxidizing gases might be attributed to the formation of p–n heterojunctions, leading to the formation of a carrier depletion region and modification of the electrical characteristics of the device with an enhancement in gas sensor characteristics.

Author Contributions: Zafer Ziya Öztürk and Serkan Büyükköse conceived and designed the experiments; Onur Alev, Alp Kılıç, and Çiğdem Çakırlar performed the experiments; Onur Alev and Serkan Büyükköse analyzed the data; Onur Alev wrote the paper. All authors discussed the results and contributed to the final manuscript.

Conflicts of Interest: The authors declare no conflict of interest.

References

1. Eranna, G.; Joshi, B.C.; Runthala, D.P.; Gupta, R.P. Oxide Materials for Development of Integrated Gas Sensors—A Comprehensive Review. *Crit. Rev. Solid State Mater. Sci.* **2004**, *29*, 111–188. [CrossRef]
2. Arafat, M.M.; Dinan, B.; Akbar, S.A.; Haseeb, A.S.M.A. Gas Sensors Based on One Dimensional Nanostructured Metal-Oxides: A Review. *Sensors* **2012**, *12*, 7207–7258. [CrossRef] [PubMed]
3. Sun, Y.-F.; Liu, S.-B.; Meng, F.-L.; Liu, J.-Y.; Jin, Z.; Kong, L.-T.; Liu, J.-H. Metal Oxide Nanostructures and Their Gas Sensing Properties: A Review. *Sensors* **2012**, *12*, 2610–2631. [CrossRef] [PubMed]
4. Liu, Y.; Li, G.; Mi, R.; Deng, C.; Gao, P. An environment-benign method for the synthesis of p-NiO/n-ZnO heterostructure with excellent performance for gas sensing and photocatalysis. *Sens. Actuators B Chem.* **2014**, *191* (Suppl. C), 537–544. [CrossRef]

5.   Cui, G.; Gao, L.; Yao, B.; Wang, S.; Zhang, P.; Zhang, M. Electrochemistry of CuO/In_2O_3 p–n heterojunction nano/microstructure array with sensitivity to H_2 at and below room-temperature. *Electrochem. Commun.* **2013**, *30*, 42–45. [CrossRef]

6.   Miller, D.R.; Akbar, S.A.; Morris, P.A. Nanoscale metal oxide-based heterojunctions for gas sensing: A review. *Sens. Actuators B Chem.* **2014**, *204*, 250–272. [CrossRef]

7.   Tomer, V.K.; Duhan, S. Ordered mesoporous Ag-doped TiO_2/SnO_2 nanocomposite based highly sensitive and selective VOC sensors. *J. Mater. Chem. A* **2016**, *4*, 1033–1043. [CrossRef]

8.   Li, Z.; Haidry, A.A.; Gao, B.; Wang, T.; Yao, Z. The effect of Co-doping on the humidity sensing properties of ordered mesoporous TiO_2. *Appl. Surf. Sci.* **2017**, *412*, 638–647. [CrossRef]

9.   Korotcenkov, G.; Cho, B.K. Metal oxide composites in conductometric gas sensors: Achievements and challenges. *Sens. Actuators B Chem.* **2017**, *244*, 182–210. [CrossRef]

10. Wetchakun, K.; Samerjai, T.; Tamaekong, N.; Liewhiran, C.; Siriwong, C.; Kruefu, V.; Wisitsoraat, A.; Tuantranont, A.; Phanichphant, S. Semiconducting metal oxides as sensors for environmentally hazardous gases. *Sens. Actuators B Chem.* **2011**, *160*, 580–591. [CrossRef]

11. Yamazoe, N.; Shimanoe, K. Roles of Shape and Size of Component Crystals in Semiconductor Gas Sensors I. Response to Oxygen. *J. Electrochem. Soc.* **2008**, *155*, J85–J92. [CrossRef]

12. Mirzaei, A.; Leonardi, S.G.; Neri, G. Detection of hazardous volatile organic compounds (VOCs) by metal oxide nanostructures-based gas sensors: A review. *Ceram. Int.* **2016**, *42*, 15119–15141. [CrossRef]

13. Gönüllü, Y.; Haidry, A.A.; Saruhan, B. Nanotubular Cr-doped TiO_2 for use as high-temperature NO_2 gas sensor. *Sens. Actuators B Chem.* **2015**, *217*, 78–87. [CrossRef]

14. Bayata, F.; Saruhan-Brings, B.; Ürgen, M. Hydrogen gas sensing properties of nanoporous Al-doped titania. *Sens. Actuators B Chem.* **2014**, *204*, 109–118. [CrossRef]

15. Galstyan, V. Porous TiO_2-Based Gas Sensors for Cyber Chemical Systems to Provide Security and Medical Diagnosis. *Sensors* **2017**, *17*, 2947. [CrossRef] [PubMed]

16. Wöllenstein, J.; Burgmair, M.; Plescher, G.; Sulima, T.; Hildenbrand, J.; Böttner, H.; Eisele, I. Cobalt oxide based gas sensors on silicon substrate for operation at low temperatures. *Sens. Actuators B Chem.* **2003**, *93*, 442–448. [CrossRef]

17. Lee, K.K.; Chin, W.S.; Sow, C.H. Cobalt-based compounds and composites as electrode materials for high-performance electrochemical capacitors. *J. Mater. Chem. A* **2014**, *2*, 17212–17248. [CrossRef]

18. Li, W.Y.; Xu, L.N.; Chen, J. Co_3O_4 Nanomaterials in Lithium-Ion Batteries and Gas Sensors. *Adv. Funct. Mater.* **2005**, *15*, 851–857. [CrossRef]

19. Vladimirova, S.; Krivetskiy, V.; Rumyantseva, M.; Gaskov, A.; Mordvinova, N.; Lebedev, O.; Martyshov, M.; Forsh, P. Co_3O_4 as p-Type Material for CO Sensing in Humid Air. *Sensors* **2017**, *17*, 2216. [CrossRef] [PubMed]

20. Sennik, E.; Kilinc, N.; Ozturk, Z.Z. Electrical and VOC sensing properties of anatase and rutile TiO_2 nanotubes. *J. Alloy. Compd.* **2014**, *616*, 89–96. [CrossRef]

21. Şennik, E.; Alev, O.; Öztürk, Z.Z. The effect of Pd on the H_2 and VOC sensing properties of TiO_2 nanorods. *Sens. Actuators B Chem.* **2016**, *229*, 692–700. [CrossRef]

22. Zhou, W.-J.; Zhang, J.; Xue, T.; Zhao, D.-D.; Li, H.-L. Electrodeposition of ordered mesoporous cobalt hydroxide film from lyotropic liquid crystal media for electrochemical capacitors. *J. Mater. Chem.* **2008**, *18*, 905–910. [CrossRef]

23. Şennik, E.; Çolak, Z.; Kılınç, N.; Öztürk, Z.Z. Synthesis of highly-ordered TiO_2 nanotubes for a hydrogen sensor. *Int. J. Hydrog. Energy* **2010**, *35*, 4420–4427. [CrossRef]

24. Cao, C.; Hu, C.; Shen, W.; Wang, S.; Wang, J.; Tian, Y. Fabrication of a novel heterostructure of Co_3O_4-modified TiO_2 nanorod arrays and its enhanced photoelectrochemical property. *J. Alloy. Compd.* **2013**, *550*, 137–143. [CrossRef]

25. Liang, Y.Q.; Cui, Z.D.; Zhu, S.L.; Li, Z.Y.; Yang, X.J.; Chen, Y.J.; Ma, J.M. Design of a highly sensitive ethanol sensor using a nano-coaxial p-Co_3O_4/n-TiO_2 heterojunction synthesized at low temperature. *Nanoscale* **2013**, *5*, 10916–10926. [CrossRef] [PubMed]

26. Kumar, D.; Chen, M.S.; Goodman, D.W. Characterization of ultra-thin TiO_2 films grown on Mo(112). *Thin Solid Films* **2006**, *515*, 1475–1479. [CrossRef]

27. Wu, Y.; Garfunkel, E.; Madey, T.E. Growth and oxidation of ultra-thin Al films on the Re(0001) surface. *Surf. Sci.* **1996**, *365*, 337–352. [CrossRef]

28. Wu, Y.; Tao, H.-S.; Garfunkel, E.; Madey, T.E.; Shinn, N.D. Growth, interfacial alloying, and oxidation of ultra-thin Al films on Ru(0001). *Surf. Sci.* **1995**, *336*, 123–139. [CrossRef]

29. Şahin, Y.; Öztürk, S.; Kılınç, N.; Kösemen, A.; Erkovan, M.; Öztürk, Z.Z. Electrical conduction and NO$_2$ gas sensing properties of ZnO nanorods. *Appl. Surf. Sci.* **2014**, *303*, 90–96. [CrossRef]

30. Wang, C.; Yin, L.; Zhang, L.; Xiang, D.; Gao, R. Metal Oxide Gas Sensors: Sensitivity and Influencing Factors. *Sensors* **2010**, *10*, 2088–2106. [CrossRef] [PubMed]

31. Gu, H.; Wang, Z.; Hu, Y. Hydrogen Gas Sensors Based on Semiconductor Oxide Nanostructures. *Sensors* **2012**, *12*, 5517–5550. [CrossRef] [PubMed]

32. Kim, H.-J.; Lee, J.-H. Highly sensitive and selective gas sensors using p-type oxide semiconductors: Overview. *Sens. Actuators B Chem.* **2014**, *192*, 607–627. [CrossRef]

33. Ju, D.; Xu, H.; Qiu, Z.; Guo, J.; Zhang, J.; Cao, B. Highly sensitive and selective triethylamine-sensing properties of nanosheets directly grown on ceramic tube by forming NiO/ZnO PN heterojunction. *Sens. Actuators B Chem.* **2014**, *200*, 288–296. [CrossRef]

34. Xu, H.; Ju, D.; Li, W.; Gong, H.; Zhang, J.; Wang, J.; Cao, B. Low-working-temperature, fast-response-speed NO$_2$ sensor with nanoporous-SnO$_2$/polyaniline double-layered film. *Sens. Actuators B Chem.* **2016**, *224*, 654–660. [CrossRef]

35. Ju, D.; Xu, H.; Xu, Q.; Gong, H.; Qiu, Z.; Guo, J.; Zhang, J.; Cao, B. High triethylamine-sensing properties of NiO/SnO$_2$ hollow sphere P–N heterojunction sensors. *Sens. Actuators B Chem.* **2015**, *215*, 39–44. [CrossRef]

36. Na, C.W.; Woo, H.-S.; Kim, I.-D.; Lee, J.-H. Selective detection of NO$_2$ and C$_2$H$_5$OH using a Co$_3$O$_4$-decorated ZnO nanowire network sensor. *Chem. Commun.* **2011**, *47*, 5148–5150. [CrossRef] [PubMed]

37. Liu, L.; Guo, C.; Li, S.; Wang, L.; Dong, Q.; Li, W. Improved H$_2$ sensing properties of Co-doped SnO$_2$ nanofibers. *Sens. Actuators B Chem.* **2010**, *150*, 806–810. [CrossRef]

38. Liu, P.F.; Yang, S.; Zheng, L.R.; Zhang, B.; Yang, H.G. Electrochemical etching of α-cobalt hydroxide for improvement of oxygen evolution reaction. *J. Mater. Chem. A* **2016**, *4*, 9578–9584. [CrossRef]

39. Dieter, K. Function and applications of gas sensors. *J. Phys. D Appl. Phys.* **2001**, *34*, R125.

40. Wang, Z.; Li, Z.; Sun, J.; Zhang, H.; Wang, W.; Zheng, W.; Wang, C. Improved Hydrogen Monitoring Properties Based on p-NiO/n-SnO$_2$ Heterojunction Composite Nanofibers. *J. Phys. Chem. C* **2010**, *114*, 6100–6105. [CrossRef]